Cement and Concrete Composites 139 (2023) 105004

Contents lists available at ScienceDirect

Cement and Concrete Composites

journal homepage: www.elsevier.com/locate/cemconcomp

Bonding mechanisms and micro-mechanical properties of the interfacial transition zone (ITZ) between biochar and paste in carbon-sink cement-based composites

Xiaohong Zhu [a], Yuying Zhang [a], Liang Chen [a], Lei Wang [b], Bin Ma [c], Jiaqi Li [d], Chi Sun Poon [a,e], Daniel C.W. Tsang [a,b,*]

[a] Department of Civil and Environmental Engineering, The Hong Kong Polytechnic University, Hung Hom, Kowloon, Hong Kong, China
[b] State Key Laboratory of Clean Energy Utilization, Zhejiang University, Hangzhou, 310027, China
[c] Laboratory for Waste Management, Nuclear Energy and Safety, Paul Scherrer Institute, 5232, Villigen, Switzerland
[d] Atmospheric, Earth, and Energy Division, Lawrence Livermore National Laboratory, United States
[e] Research Centre for Resources Engineering Towards Carbon Neutrality, The Hong Kong Polytechnic University, Hung Hom, Kowloon, Hong Kong, China

ARTICLE INFO

Keywords:
Carbon sequestration
Engineered biochar
Hydration products
Deformation characteristics
Nano-indentation

ABSTRACT

A better understanding of the interfacial transition zone (ITZ) in biochar-augmented carbon-negative cementitious materials can facilitate their potential applications. This study illustrated the key chemical and mechanical features of such a region in Portland cement using backscattered electron microscopy-energy dispersive X-ray analysis (BSEM-EDX), nano-indentation, and X-ray computed tomography (X-CT). It was found that a significant 'wall effect' was identified at the side-edge of biochar, where the degree of hydration and the porosity significantly increased. The biochar was integrated into the hardened cement matrix via a layer of Ca-rich hydration products mainly composed of AFm phases, CH and C–S–H gels. Regarding the mechanical behaviour, the biochar showed a typical viscous-elastic (VE) deformation mode at the nano/micro scale, whereas the hardened cement was a typical plastic-elastic (PE) material. Therefore, the value of the hardness of biochar was not accurate under limited plastic deformation. The distinct differences in deformation resulted in the largest residual deformation (i.e., plasticity) of the hardened cement after indentation when compared to ITZ and biochar regions, whereas the ITZ maintained a lower value due to well connection with biochar. These microstructural characteristics partially explained the higher compressive strength of biochar-cement composites than previously expected.

1. Introduction

CO_2 emissions have increased gradually over the century, triggering extreme weather events and posing potential threats to the environment and human health [1,2]. As concrete production is associated with approximately 8% of global anthropogenic CO_2 emissions annually [3,4], it is inevitable to seek low-carbon-footprint or even carbon-negative concrete products [5,6]. Recently, carbon-negative concrete has been developed by incorporating a large volume of biochar as the carbon sink [7]. The invention of such a carbon-negative concrete product shows promising economic profits and environmental benefits in the construction industry [8], turning conventional high-carbon emission building materials into a sustainable carbon tank.

One of the most important materials used for carbon sequestration is biochar, derived from the pyrolysis of a wide range of biomass under a limited oxygen environment [9]. The life cycle analysis (LCA) of biochar shows that 2.0–3.3 tonnes of CO_{2eq} could be stabilised by 1 tonne of biochar application [10,11], which is thus recommended by the IPCC (Intergovernmental Panel on Climate Change) as the promising material to achieve carbon neutrality [2]. Using biochar as a portion of aggregate in concrete, up to 59 kg CO_2 could be sequestered in each tonne of concrete, which corresponds to the overall profit of 35.4 USD per cubic metre of concrete when considering the carbon-trading credit [7,8]. In addition to the promising carbon-negative nature, other value-added benefits to concrete products, such as shrinkage mitigation [12], acoustic and thermal insulation [13–15], and potential immobilisation of toxic elements [16–18], could be achieved by adding various contents of functional biochar. Therefore, biochar can play as a multi-role

* Corresponding author. Department of Civil and Environmental Engineering, The Hong Kong Polytechnic University, Hung Hom, Kowloon, Hong Kong, China.
E-mail address: dan.tsang@polyu.edu.hk (D.C.W. Tsang).

https://doi.org/10.1016/j.cemconcomp.2023.105004
Received 13 December 2022; Received in revised form 15 February 2023; Accepted 26 February 2023
Available online 3 March 2023
0958-9465/

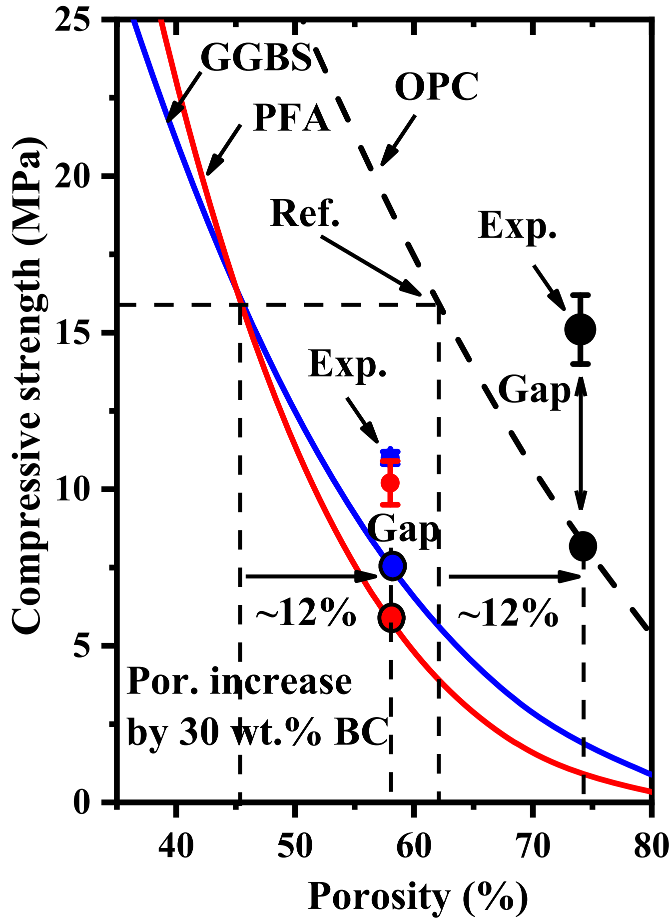

Fig. 1. Estimated reduction of compressive strength of OPC (black dash line) and GGBS/PFA (blue/red solid lines) blended mortar based on an empirical formula derived from experimental observations [19]. The Ref. (i.e., plain mortars) and Exp. (i.e., biochar-added mortars) are the experimental data from Ref. [7]. The addition of 30 wt% biochar (BC) is estimated to increase 12% porosity theoretically based on the raw materials used in Ref. [7] (See **Note S1** for the estimation). The blue, red, and black-filled circles are the theoretical values of biochar-augmented mortar, whereas the corresponding ones with error bars are experimental observations. The starting compressive strength of GGBS/FA mortars is assumed to be the same as that of OPC, even though they are expected to be lower as indicated by the empirical formula. The 'Gap' demonstrated a higher compressive strength than expected. (For interpretation of the references to colour in this figure legend, the reader is referred to the Web version of this article.)

additive in concrete, and its working mechanisms in hardened cementitious materials necessitate in-depth studies.

Even though the accelerating effect of biochar on cement hydration has been experimentally proved (see cf. Fig. 1 in Ref. [7] for the isothermal calorimetry curves), introducing pores from the biochar addition might be a concern about the potential reduction of mechanical properties. The classic porosity-strength relationships in ordinary Portland cement (OPC) mortar and ground granulated blast-furnace slag (GGBS)/pulverised fly ash (PFA) blended mortar was established by the empirical formulae [19] (Fig. 1), which can be used for estimating the reduction of compressive strength for the biochar-augmented cement composites. Clearly, the experimental observations confirmed the superior mechanical properties (as indicated by the 'Gap' in Fig. 1) than the estimated values based solely on the increased porosity. This is abnormal because the interfacial transition zone (ITZ) forms when aggregates are incorporated into the pastes [20,21], which has been considered to have a significantly negative influence on concrete properties for many years. Traditionally, the co-existence of higher porosity [21] and more defects [22] in the ITZ between aggregate and cement matrix would result in lower compressive strength and higher permeability of concrete [23]. However, the bonding between biochar and cement matrix might be enhanced, possibly contributing to the higher compressive strength (the 'Gap' in Fig. 1) of biochar-cement composite. This inference was partially evidenced by the X-ray computed tomography (CT) study (see cf. Fig. 8 in Ref. [7]), showing significantly more defects and pores surrounding the fine aggregates (i.e., the ITZ) in the normal mortar than those in the biochar-cement composite. Although a previous study [7] proved that the hydration of cement was accelerated, it might not essentially indicate that the compressive strength of the mortar would be higher than expected (Fig. 1). Therefore, an in-depth understanding of such a zone is essential.

This study aims to unveil and elucidate the interaction mechanisms between biochar and cement matrix from the point of view of chemical compositions and physical properties. The localised features, including chemical compositions and porosity variations, surrounding the biochar were evaluated through backscattering electron microscopy (BSEM) combined with the energy dispersive X-ray analysis (EDX). The micromechanical properties of ITZ were explored using nano-indentation in joint with the finite element model (FEM). The three-dimensional distribution of the featured area was illustrated by X-ray CT to support the two-dimensional findings.

2. Experimental details

2.1. Materials and sample preparations

The CEM I Portland cement was supplied by Hong Kong Green Island cement company, and the biochar derived from wood waste (*Acacia confusa and Celtis sinensis*) pyrolysed at 700 °C was provided by Kadoorie Farm in Hong Kong. The detailed raw materials' properties, casting and curing procedures were documented in Ref. [7]. Briefly, the biochar used in this study was screened to the size of 0–5 mm. which had a surface area of 124.7 m^2/g and an average pore diameter of 5.24 nm (BET method). The pre-soaked biochar was used to replace the fine aggregate in the mortar. The sample used in the current study was marked as 30BC in Ref. [7] (See Table3 in cf. [7]) with the total replacement of the fine aggregate by biochar at the water-to-binder ratio of 0.30. The mixture design of this sample was 50 wt% CEM I cement and 50 wt% pre-soaked biochar.

A piece of the mortar sample ($1 \times 1 \times 1$ cm^3) was cored from the block and impregnated with epoxy (Buehler EpoxiCure 2, USA). The vacuum chamber (Cast N′ Vac, Buehler, USA) was used to ensure the open voids were filled by the epoxy resin and remove air bubbles. The as-prepared sample was then polished with SiC papers (#600 and #1200 grit) until all the hardened epoxy on the sample's surface was removed. After, the sample was polished by the polishing cloth (MicroCloth/ChemoMet, Buehler, USA) with 1 and 0.05 μm polished solutions (MicroPolish II Alumina, Buehler, USA) for around 1 h under the loading of 2 lb. The final process was using the isopropanol to wash the residual alumina on the sample in the ultrasonic bath for around 20 min. The surface roughness of the ITZ area was checked by scanning probe microscopy (SPM) equipped in the Nano-indentation system (Hysitron TI Premier, Bruker). The average Root Mean Square (RMS) of a surface measured by microscopic peaks and valleys can be maintained at less than 30 nm, as shown by the example given in Fig. S1.

2.2. Characterisation techniques

The as-polished sample was used for both nano-indentation and BSEM-EDX tests. Due to the lower strength of our sample [7], a trapezoidal loading scheme with a maximum loading of 1000 μN (5 s loading – 2 s holding – 5 s unloading) was used during nano-indentation. In this study, the nano-indentation was evenly performed over a grid of 10×10 points in an area of 100 μm. The Berkovich-shape diamond indenter was

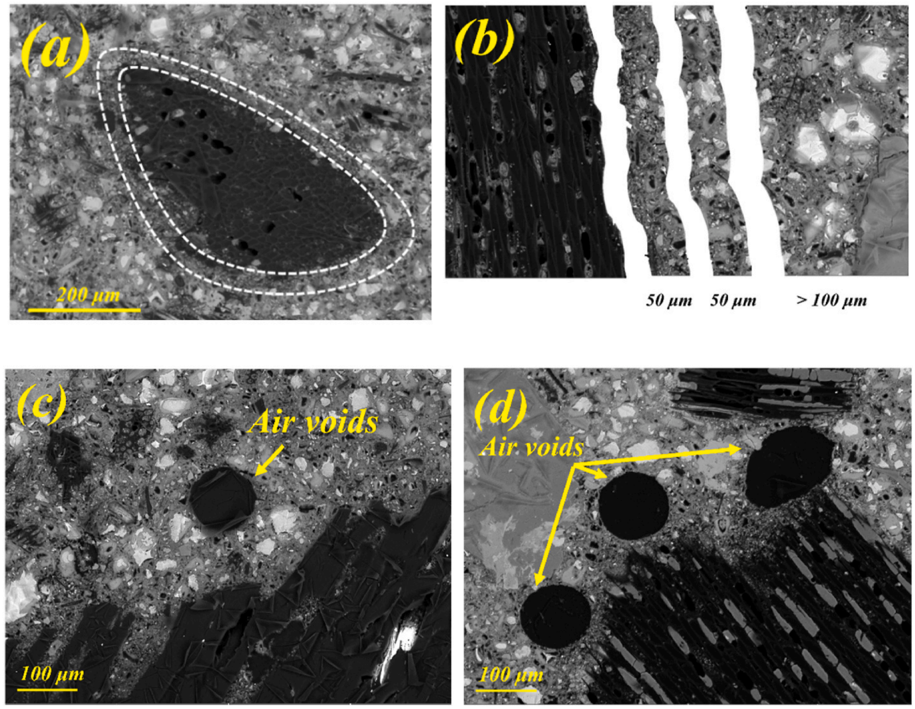

Fig. 2. ITZ area (~50 μm) surrounding the side-edge of a biochar particle section (~700 × 300 μm^2): (a) overall particle; (b) closer observation and segmentation of the localised feature; (c) and (d) BSEM images showing the air voids exchanged from the inner pores of top-edge biochar.

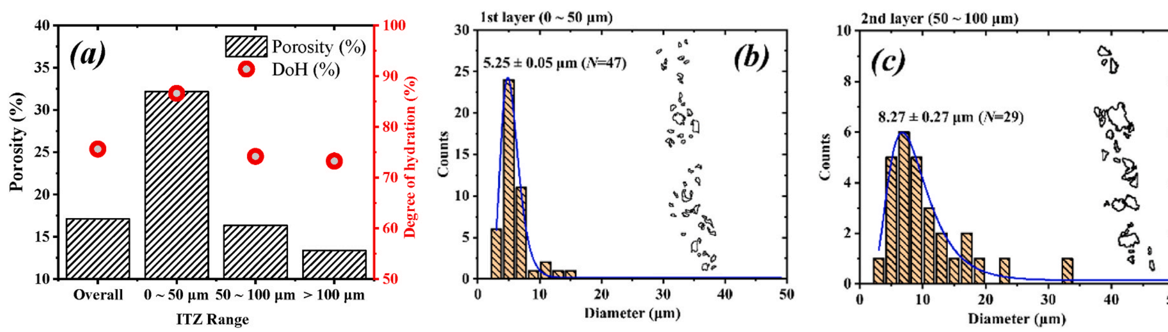

Fig. 3. (a) Degree of hydration of clinkers and porosity of cement matrix along the biochar-cement ITZ shown in Fig. 2b; (b)–(c) Particle size distribution of unreacted clinkers of the first (0–50 μm) and second (50–100 μm) layer in ITZ. The data processing can be found in Fig. S4.

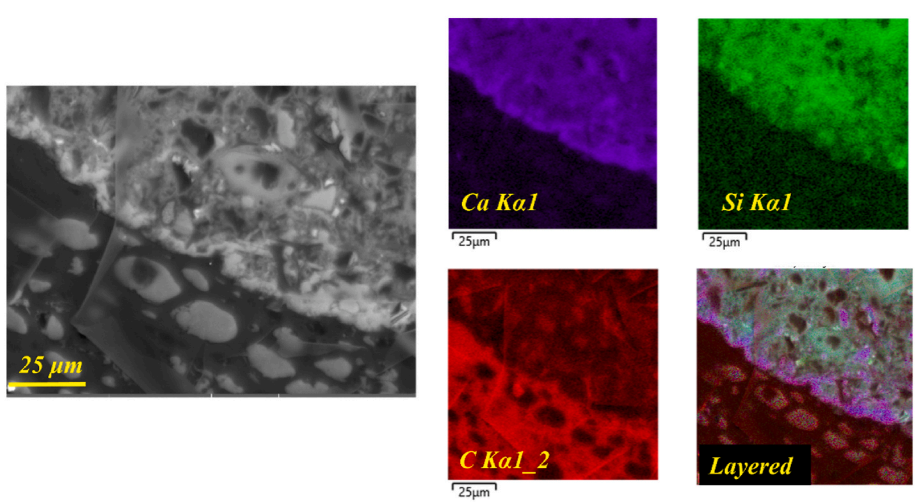

Fig. 4. Interactions between biochar and cement: ~1.89 μm thickness of calcium hydroxide crystal, illustrated by BSEM-EDX mapping.

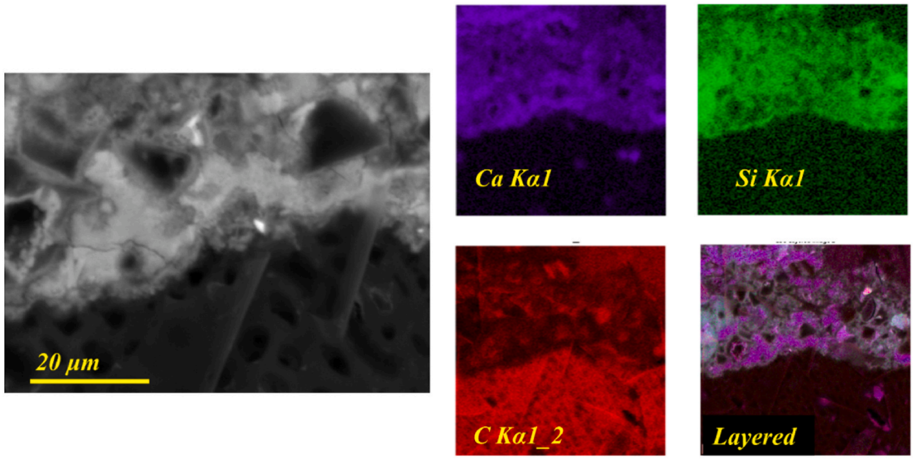

Fig. 5. Interactions between biochar and cement: ~2.00 μm thickness of C–S–H gel between the biochar and the calcium hydroxide crystals (~5–10 μm thickness), illustrated by BSEM-EDX mapping.

used to minimise the pile-up effect [24,25]. The internal stress distribution of the featured loading-displacement process was performed in ABAQUS® using FEM to show the mechanical behaviours of different regions suffering from the nano-indentation. The geometry of the Berkovich-shape indenter and the contact surface mesh was built according to the existing studies [26]. The basics of continuum micromechanics related to the process of nano-indentation can be found in the literature [27–29]. The input data (Fig. S2) were from experimental observations of loading-displacement curves with the measured elastic modulus (*Er*), and axisymmetric conditions were used for the calculation. The internal stress distribution could be visually illustrated with the experimental input data. In addition, in order to overcome the convergence problem of the viscous-elastic deformation, 0.001 of increment size with the quasi-Newton method was used during the simulation.

The as-polished sample was carbon-coated and observed under the backscattered mode SEM (VEGA3, TESCAN, Czech Republic) equipped with an EDX (Ultim Extreme, Oxford Instruments, UK). The images were taken at the accelerating voltage of 20 kV and a beam current of 1–2 nA. The EDX points were collected at a working distance of 15 mm, with a live time of 20 s and the counts per analysis of 100,000. The EDX-mappings were also acquired at the working distance of 15 mm, with a resolution of 2048, a processing time of 5 s, and a pixel dwell time of 100 μs. The mapping was stopped until the precise elemental distribution could be visually observed. The BSEM images were processed using self-coded Python programmes based on the grey scale distribution. An example was given in Fig. S3 to show the segmenting and painting processes of the BSEM image of ITZ using an arbitrary threshold method [20,22]. The strip analysis (Fig. S4) was then performed along the boundary of biochar to estimate the variations in the physical properties of the cement matrix.

A cylindrical (Φ 20 × 50 mm) biochar-cement composite was used for X-ray CT scanning (Phoenix v|tome|x s, GE Inspection Technologies, USA) equipped with a 240 kV/320 W microfocus tube. A long scanning time (2000 projections and 10 s per projection) enabled a resolution of 2 μm. The Java-based programme re-constructed the X-ray tomography images into three-dimensional models [30].

3. Results and discussion

3.1. 'Wall effect' and 'dilution effect' of ITZ surrounding biochar

The so-called 'wall effect' due to the presence of the flat aggregate surface has long been known as the origin of the ITZ formation [21,22]. The difference in the size of aggregate and cement grains resulted in the disruption of particle packing in the ITZ, forming the distinct 'shells' that progressively changed normal to the surface of aggregate [31]. However, compared to normal aggregate, biochar showed a significantly different microstructure, which preserved the features of wood that has the flat longitudinal side (i.e., side-edge) and the porous transverse cross-section (i.e., top-edge) [32,33]. As expected, the differences in the ITZ of the side- and top-edges of biochar can be visualised in the BSEM images (Fig. 2).

The transverse cross-section of biochar was entirely preserved as shown by the example (~700 × 300 μm^2) in Fig. 2a, where a clear strip of ITZ (~50 μm as indicated by the white dash border) surrounding the side-edge of biochar could be distinguished. This layer of ITZ could be more vividly illustrated by the strip-analysis [21,22,34,35] with an interval of 50 μm as shown in Fig. 2b. The internal layer that was closest to the biochar showed fewer and smaller brighter particles than the bulk pastes, which confirms that the same 'wall effect' happened between the side-edge of biochar and the matrix. Regarding the ITZ in the top-edge (Fig. 2c and d), similar darker regions due to the higher degree of hydration of clinker were observed, which was because the pre-soaked biochar supplied additional water that preferably escaped from the top side, resulting in the locally higher water-to-cement ratio (i.e., dilution effect). In addition, some entrapped air voids were found. This was attributed to the air in the biochar, which was released due to the exchange of water and fresh paste before its setting. Even though the biochar was pre-soaked, the physical adsorption between its abundant functional groups and gas molecules may preserve air bubbles inside the pores [36]. In contrast, the side-edge of biochar would form the water film during pre-soaking, enhancing the 'wall effect' in this region.

Fig. 3 quantifies the degree of hydration (DoH) of clinker phases, porosity, and particle size distribution of unreacted clinker according to strip-analysis shown in Fig. 2b. The overall DoH of the selected area (up to ~ 250 μm normal to the side-edge of biochar) was 75.6%, which was higher than the overall DoH estimated by ^{29}Si nuclei magnetic resonance (NMR) [7]. Two reasons could account for this phenomenon: firstly, the ^{29}Si NMR ignored the hydration of aluminates in the clinkers; secondly, the pre-soaked biochar had more free water attached to the surface of its side-edge, which increased the local water-to-binder ratio. Regarding the stepwise change of DoH, which reached 86.6% in the ITZ zone (~50 μm normal to biochar) and gradually decreased to 74.2% (50–100 μm) and 73.2% (>100 μm) with increasing distance, respectively. Meanwhile, the higher water-to-binder ratio in the ITZ resulted in a higher porosity of 32.2%, gradually reducing to 16.3% and 13.4% in the other two regions. The statistical analysis showed that the mean size of the unreacted clinker was 5.25 ± 0.05 μm (N = 47), which increased to 8.27 ± 0.27 μm (N = 29). All the experimental shreds of evidence confirmed

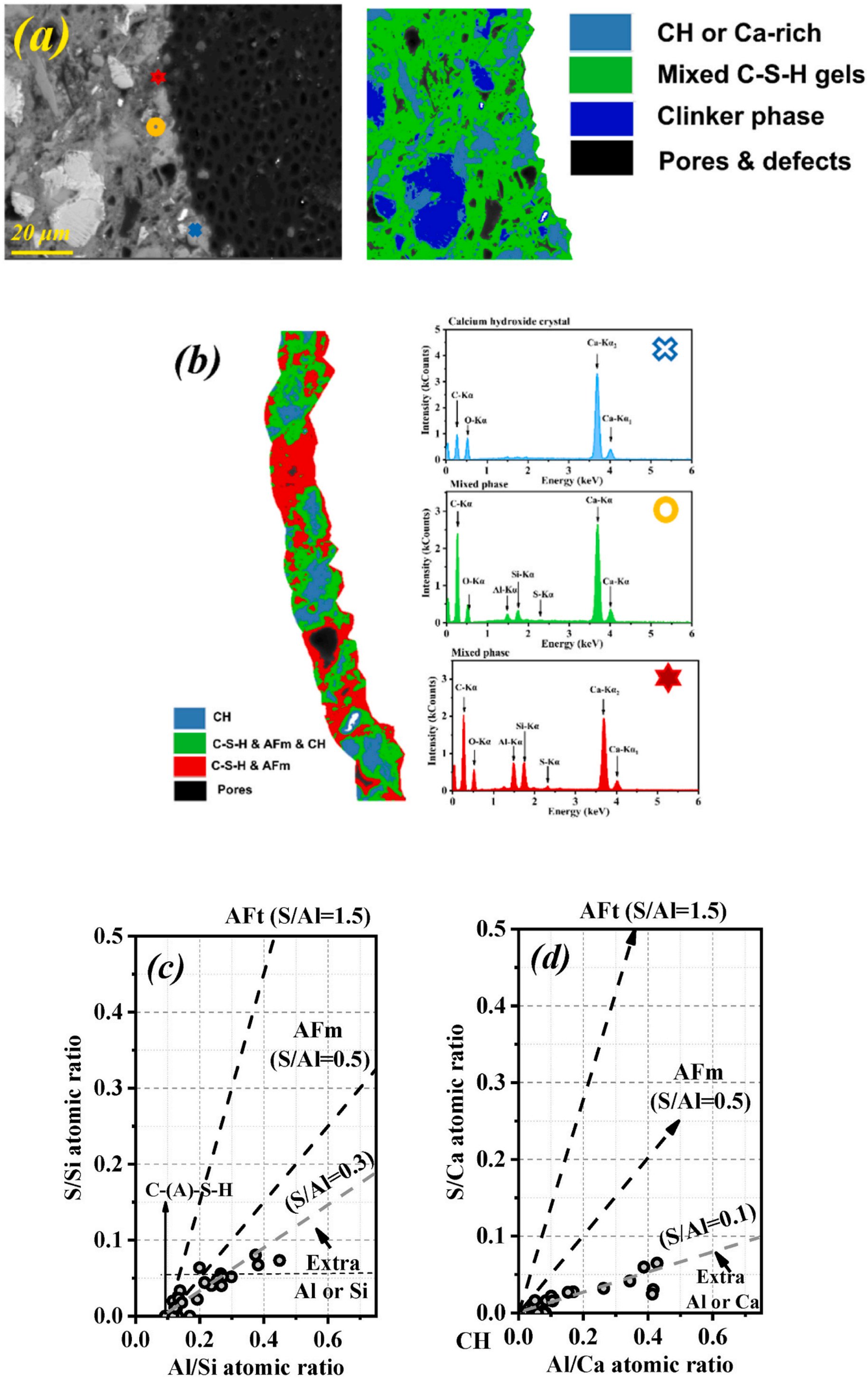

Fig. 6. Interactions between biochar and cement: (a) ~ 5 μm thickness of mixture of Ca-rich phase and C–S–H gel; (b) segments of the interfacial zone (~5 μm) and the corresponding EDX spectra; (c) and (d) distribution of chemical compositions from BSEM-EDX.

that the 'wall effect' happened at the side-edge of biochar, which is similar to the ITZ of aggregate in concrete [21,22].

3.2. Localised bonding mechanisms between biochar and cement matrix

As shown in Figs. 4 and 5, a higher magnification (× 3000) was needed to characterise the local bonding features of biochar and cement matrix. The BSEM images provide the compositional information (i.e., average atomic number) of the regions of interest, where the brighter area corresponds to the heavier or denser compositions (i.e., higher average atomic number) [37]. In both Figs. 4 and 5, the dark and porous regions were the biochar, which closely connected to the brighter grey OPC matrix via a layer of the significantly brighter strips. The distinctive difference between Figs. 4 and 5 is that the former was connected directly via the ~1.89 μm brightest region, and the latter was connected via the ~2.00 μm grey region followed by the brightest region (~5–10 μm). The EDX mapping indicated that the brightest regions were calcium hydroxide (CH), whilst the grey region between the biochar and the CH was a layer of C–S–H gel. Such a concentration of CH was also observed in the ITZ of normal concrete; the high concentration of CH

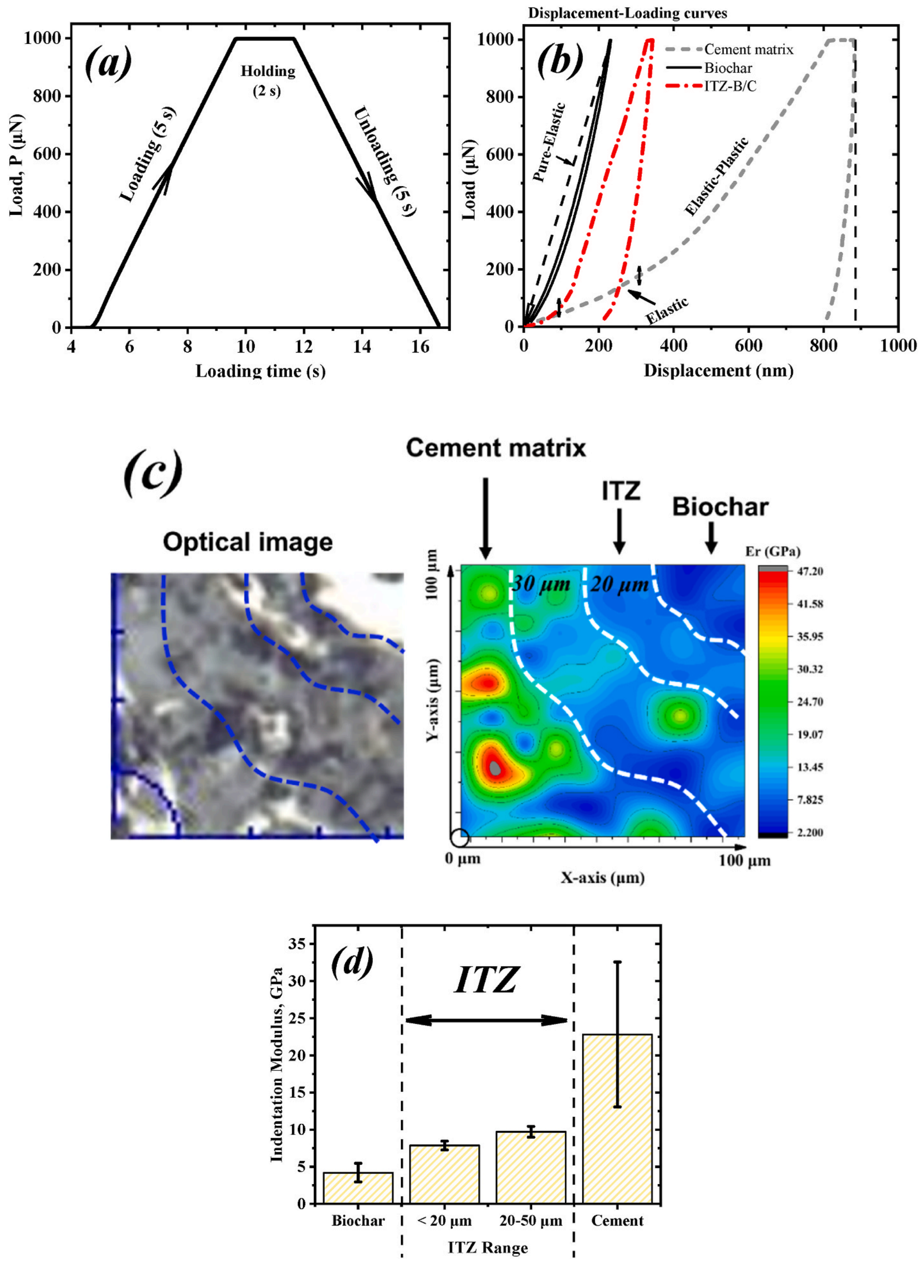

Fig. 7. Nano-indentation results of the ITZ between biochar and cement matrix: (a) loading scheme; (b) characteristic displacement-loading curves of the cement matrix, biochar, ITZ near biochar, and ITZ near the cement; (c) optical image and reduced elastic modulus (*Er*, GPa) of the ITZ; the hardness (*H*, GPa, as shown in Fig. S5) cannot be used due to the mechanical characteristics of biochar; and (d) average *Er* of the regions separated in (c).

was only observed randomly around the biochar [21]. Nevertheless, two unique bonding mechanisms, i.e., via CH or a layer of C–S–H gel, can be identified between biochar and the cement matrix. The reasons for the formation of this Ca-rich layer should be attributed to the functional groups on the surface of biochar (e.g., –OH, –COOH) [36], where the Ca ions can serve as the bridge in the ITZ that further provides the nucleation sites for the growth of CH (Fig. 4). Similarly, biochar can interact with kaolinite through the Ca-bridge to enhance its stability in soil modification [38]. Although some regions were connected via $Si(OH)_4^{4-x}$ to the cement matrix (Fig. 5), it was unavoidable to form a layer of Ca-rich hydration products in the ITZ.

Fig. 6 reveals the typical layer of the Ca-rich region containing mixed hydration products in the ITZ for further analysis. The typical hydration products were colour-painted (Fig. 6a) according to the grey scale of the BSEM image (see Fig. S3 for the detailed example) [20,21]. Clearly, CH (or Ca-rich hydration products) were randomly and distributed surrounding the biochar, but the mixed C–S–H gel phases cannot be separated at this scale (Fig. 6a). Therefore, a layer of hydration products with 10 μm thickness closest to the biochar (Fig. 6b) was zoomed in and sliced from the BSEM image for further analysis in alignment with the EDX results (as marked in Fig. 6a).

As shown in the EDX spectra (Fig. 6b), the brightest region corresponded to pure CH (pale blue), and the intermediate and least bright regions corresponded to mixed C–S–H gel and other Ca-rich hydration products. With the decrease in brightness, the increasing trend of Si and Al could be observed, indicating the increased contents of C-(A)-S-H gel and other Al-rich hydration products. Some S could also be detected in these regions with mixed hydration products. Statistical analysis was performed to differentiate the hydration products as plotted in Fig. 6c and d.

The AFt (i.e., ettringite, $Ca_6Al_2(SO_4)_3(OH)_{12}{\cdot}26H_2O$) and S-AFm (i.e., mono-sulphoaluminate, $Ca_4Al_2O_6(SO_4)(OH)_{12}{\cdot}(6+x)H_2O$) are the

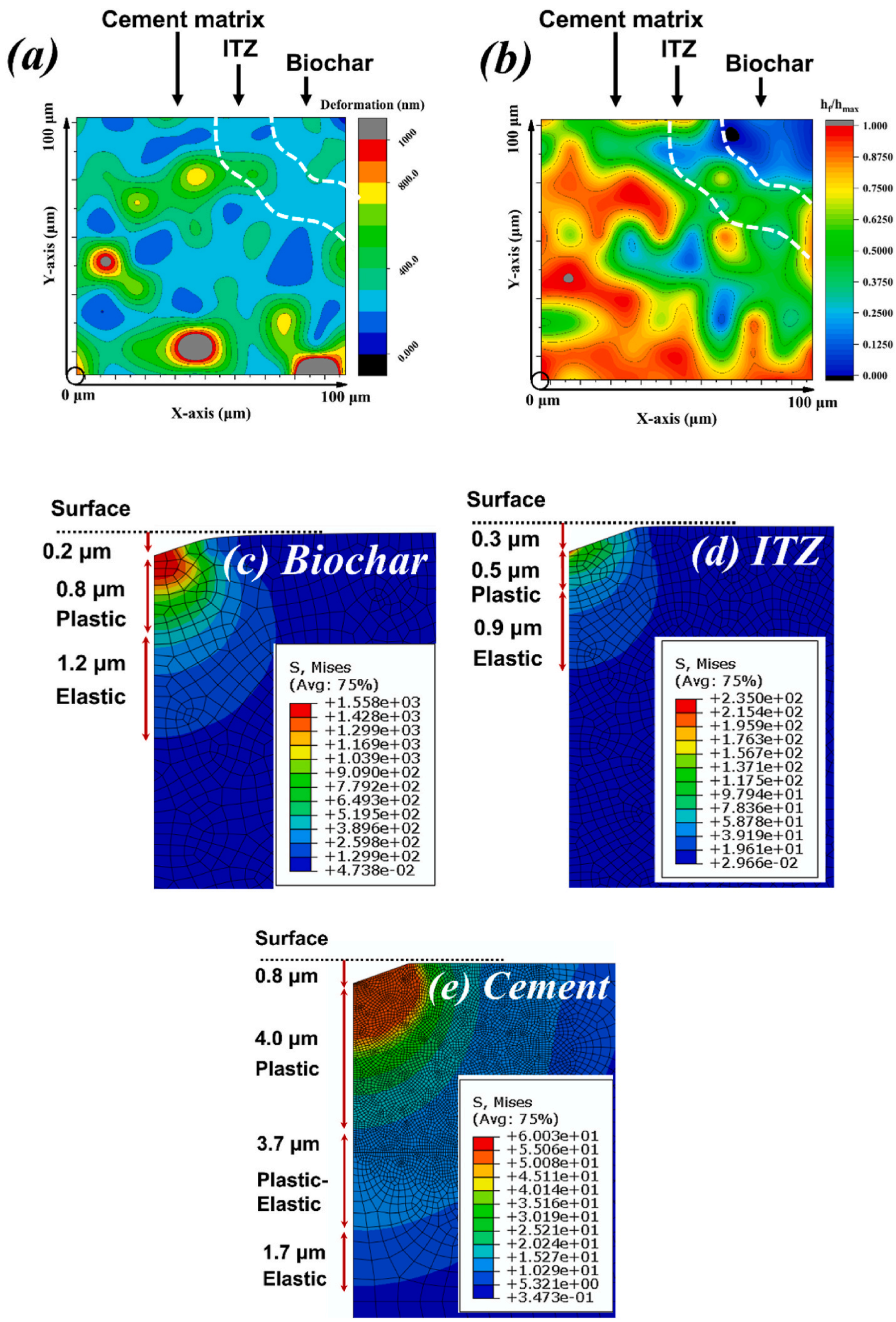

Fig. 8. Deformation and stress distribution of BC-PC composite at the micro-scale: (a) maximum deformation during the nano-indentation experiments; (b) residual deformation: the ratio of final displacement to maximum displacement (h_f/h_{max}); representative FEM showing the stress distribution and the plastic zone of (c) pure biochar; (d) ITZ; and (e) cement matrix after indentation; the corresponding simulated deformation can be found in Fig. S2. The good fitting of the simulated displacement-load curves from FEM and the experimentally determined curves can be found in Fig. S2.

two sulphate-bearing hydration products in Portland cement, resulting from the reactions of tricalcium aluminates (C_3A) and gypsum [39]. The promotion of AFt formation due to the addition of high-volume biochar was evidenced by the increase in the corresponding hydration peak in a previous study (see the peak at ~ 20 h in cf. Fig. 1b in Ref. [7]), which was ascribed to the higher water-to-cement ratio. However, the AFt peak was not as high as expected when the composites hydrated up to 28 d (see cf. Fig. 2b in Ref. [7]). The results were correct because the AFt had been converted into AFm, as evidenced by the dehydration peak in the DTG curves (see cf. Fig. 2a in Ref. [7]) within 200–330 °C, which were the dehydroxylation of OH bound to tetrahedral Al (200–240 °C) and octahedral Ca (240–330 °C), respectively [40]. However, the absence of AFm peaks in the XRD patterns (see cf. Fig. 2b in Ref. [7]) was due to insufficient signal quality, or that the crystal size was not large enough for detection [41]. More shreds of evidence of such a conversion were supported by the cluster analysis of EDX points in this study, as shown in Fig. 6c and d, which confirmed that this conversion preferred to take place in the ITZ.

The chemical compositions of the red and green regions painted according to the grey scale in Fig. 6b were further analysed. Fig. 6c plots the S/Si atomic ratio against the Al/Si atomic ratio of these chemical compositions; thus, the slope indicated the S/Al ratio. The black dash lines with a slope of 0.5 or 1.5 stand for the perfect fine-mixture of AFm/C-(A)-S-H or AFt/C-(A)-S-H, respectively, where the Si was the marker for the presence of C-A-S-H phase. The intercept point of the Al/Si axis corresponds to the Al/Si ratio in pure C-(A)-S-H in Portland cement, which was consistent with the value (~0.1) in previous studies [41–43]. However, the cluster of EDX points were slightly offset from the pure AFm/C-(A)-S-H mixed line, which formed a linear regression line with a slope of 0.3 (i.e., the grey dash line in Fig. 6c), indicating the presence of extra Si or Al-bearing phases. Similarly, Fig. 6d plots the S/Ca atomic ratio against Al/Ca atomic ratio of the same cluster EDX points, showing the relative relationship of S/Al to Ca. The black dash lines for pure AFm/CH or AFt/CH were also given in the figures (i.e., the origin point of this plot is CH instead of C-A-S-H). Again, the linear fitting line of these points was offset from the pure AFm/CH line, which formed a linear line with a slope smaller than 0.1, indicating the presence of extra Al or Ca-bearing phases. As the C-A-S-H is almost the only Si-bearing hydration product and the trace Si-AFm (i.e., hydrogarnet) needs a longer time to form [44], the offset in Fig. 6c was believed to be caused by the additional Al. Nevertheless, when the Ca and Al were abundant, the offset in Fig. 6d tended to be more pronounced. Inspection of the XRD patterns (see cf. Fig. 2b in Ref. [7]) confirmed a tiny peak at 11.2° 2θ (i.e., 7.92 Å) in 20BC and 30BC (the sample used in this study), which corresponded to the unique basal spacing of the h-AFm (i.e., C_4AH_{19}), forming at the conditions of sulphate-lacking and excessive water (see cf. Fig. 7 in Ref. [45]). Such a phase could provide a reasonable explanation for the EDX results. Other AFm phases, such as C_4AH_x, may also form but cannot be observed based on the current shreds of evidence. The h-AFm phase would form when the gypsum was entirely consumed and the local water-to-C_3A ratio was higher than 1.0 [45]. The ITZ of biochar might provide such a condition because its negatively charged surface [38,46] tended to attract positively charged ions (e.g., Ca^{2+}) or precipitate particles (i.e., C_3A in water [47–50]), whereas the sulphate ions were negatively charged. Therefore, it is conducive to the formation of a layer of C_3A-rich clinker surrounding the biochar where the water appears to be excessive.

3.3. Micro-mechanical properties of ITZ

A key problem in the ITZ study was to clarify if it has practical influences on the engineering properties of the hardened cement, of which the localised mechanical behaviour is of great importance. The nano-indentation technique enables the probe of local load-displacement behaviour at the scale of several micrometres or less [51,52]. The nano-indentation records the loading variations (P, μN) and the penetration depth (h, nm) simultaneously according to the pre-defined loading scheme (Fig. 7a). The as-formed P-h curves (Fig. 7b) demonstrated the deformation mode and thus mechanical behaviour, i.e., indentation modulus (Er, GPa, Eq. (1)) and indentation hardness (H, GPa, Eq. (2)), could be extracted based on Oliver-Pharr justification [51, 52].

$$E_r \stackrel{\text{def}}{=} \frac{\sqrt{\pi}}{2}\frac{S}{\sqrt{A_c}} \quad \text{Equation 1}$$

$$H \stackrel{\text{def}}{=} \frac{P_{max}}{A_c} \quad \text{Equation 2}$$

where S is the unloading stiffness, and A_c is the projected area estimated from the maximum displacement (h_{max}) [51].

Fig. 7b shows the P-h curves of three typical areas (i.e., biochar, ITZ, and cement matrix) in the optical image in Fig. 7c, where the bright area on the top right corner was biochar. Distinct differences could be observed in the typical curves that reflected their unique dominant deformation mode (i.e., mechanical characteristics). The P-h curves indicated that the biochar possessed the viscous-elastic (VE) mode of deformation at the nano-/micro-scale, whereas the cement matrix had the elastic-plastic (EP) mode [53]. As expected, the ITZ showed the responses in between, tending to be EP mode of deformation. The VE mode of deformation of biochar was also reported by previous studies [54–56], which depended on the type of feedstock, pyrolysis temperature, and the reaction conditions [55]. Such mechanical behaviour was related to the excellent and natural development strategies of wood at several levels of hierarchy, which could be preserved within the microstructure of biochar [54]. The cellular honeycomb-like structure that remained in the biochar could absorb the energy due to loading and provide high-directional stiffness [32,57]. In contrast, the cement paste manifested the EP deformation mode and significant creep (see the constant loading period) due to the nature of its major hydration products, C–S–H gel [58–61]. As the ITZ was mainly composed of hydrated cement, it maintained the EP deformation mode but was less damaged after indentation. This is evidence to support that the biochar was well-connected with the cement matrix, as discussed in Section 3.2, where the biochar could partially absorb the indentation energy. The reduced modulus is estimated from the contact stiffness (Eq. (1)), which can be applied for most cases (contour pattern in Fig. 7c), whereas the hardness (H, GPa) is defined as the resistance to localised plastic deformation induced during indentation [62], which is estimated by the projected area during the indentation [51,52]. This would arouse concern for the materials with VE deformation [63], especially when there was almost no plastic deformation during the loading-unloading cycle (Fig. 7b), giving an inaccurate (much higher) value of hardness as shown in Fig. S5.

Fig. 7c plots the contour pattern of the as-calculated reduced elastic modulus (Er) at the grid indentation area containing biochar, ITZ, and the cement matrix. The white dash lines mark the outline of the biochar and the as-formed ITZ within 50 μm according to the observation of BSEM (Fig. 1). Obviously, the biochar had an indentation modulus of $M = 4.20 \pm 1.25$ GPa, which agreed with the typical M value of the wood waste derived biochar [56]. Then the modulus gradually increased to 7.8–9.7 GPa in the ITZ, which was adjacent to the cement matrix with a modulus of 22.80 ± 9.76 GPa. It is noted that the standard deviation of the elastic modulus of the cement matrix was much higher than the other areas, which was caused by the highly heterogeneous hydration products composed of micro-crystals and finely mixed C–S–H gel [29, 58]. The elastic modulus of these hydration products ranged from 5 to 50 GPa (see the frequency distribution in Fig. S6), depending on the local porosity [64] and the intermixtures [29]. The lower value of M in the ITZ was attributed to the 'wall effect', resulting in a higher local water-to-binder ratio corresponding to a lower elastic modulus [64].

Deformation of the tested area was given in Fig. 8a and b along with the representative FEM simulation results (Fig. 8c–e) of the experimental P-h curves with localised material features (i.e., the experimentally determined elastic modulus and the as-formed deformation mode). The plasticity index defined as the ratio of hardness to reduced elastic modulus [65] is not applicable as the hardness value of biochar cannot be accurately determined under the current conditions. To better illustrate the material plasticity, the ratio of the final displacement to maximum displacement is calculated and defined as the residual deformation (Eq. (3)).

$$\textit{Residul deformation} \stackrel{\text{def}}{=} \frac{h_f}{h_{max}} \quad \text{Equation 3}$$

where the h_f is the final displacement (nm) and h_{max} is the maximum displacement during the indentation (nm).

The contour pattern of maximum deformation (Fig. 8a) indicated that the largest deformation mostly took place in the cement matrix region, where the elastic modulus was higher (Fig. 7c). As expected, the residual deformation (Fig. 8b) showed distinct differences between the three regions, where the biochar maintained its original shape and the hardened cement demonstrated the brittleness feature. Interestingly, the ITZ maintained moderate residual deformation due to the better connection with biochar. The FEM results can better illustrate the internal stress of the individual indentation area. At the maximum loading condition (Fig. S2), the biochar and the ITZ only showed less than 1 μm irreversible deformation, whereas the hardened cement had a plastic deformation region up to ∼4 μm. The differences were caused by the nature of the microstructure of biochar and hardened cement as explained above. Such microstructural mechanical behaviour could partially explain the higher compressive strength (Fig. 1) of the biochar-

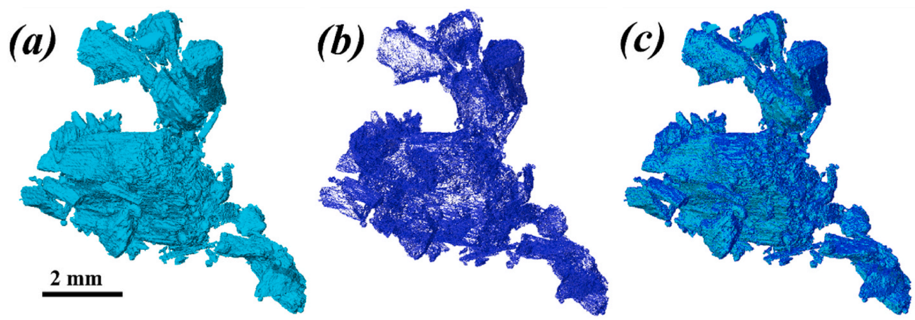

Fig. 9. Segmentation of the reconstructed 3D XCT images based on the greyscale given in Fig. S7: (a) biochar (pale blue); (b) Ca-rich layer hydration products (deep blue); and (c) combined images. (For interpretation of the references to colour in this figure legend, the reader is referred to the Web version of this article.)

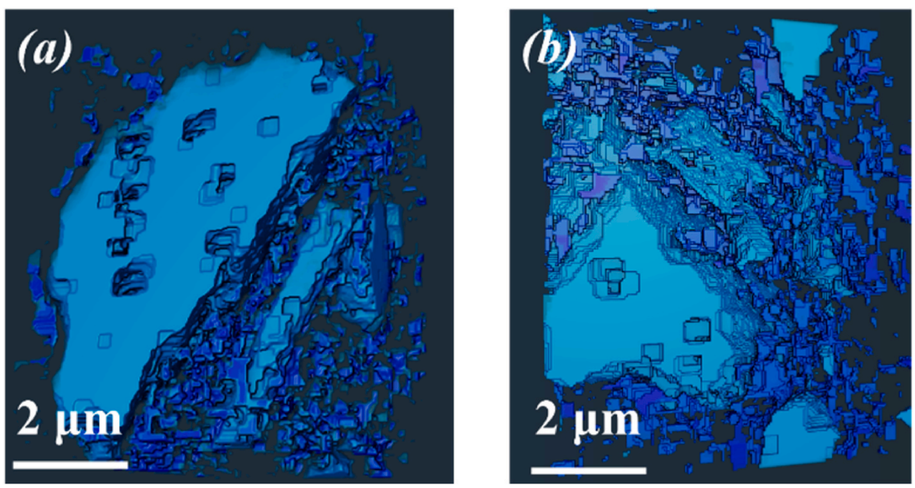

Fig. 10. Reconstructed XCT images of the small biochar particle (pale blue) with the attached Ca-rich hydration products (deep blue) using the noise-reducing algorithm: (a) top side and (b) bottom side. (For interpretation of the references to colour in this figure legend, the reader is referred to the Web version of this article.)

cement composite than expected.

3.4. *Three-dimensional reconstruction of the biochar and the Ca-rich layer*

X-ray computed tomography (X-CT) offers three-dimensional information of the hydration products surrounding the biochar, which can support the two-dimensional observations from BSEM (Section 3.2). The slice image from the CT could be used to determine the segmented grey scale as given in Fig. S7. However, it is still challenging to accurately separate the phase under the limited resolution of the X-CT equipment [66,67]. The doublet peak of the grey scale (Fig. S7b) of the CT image corresponded to the biochar and the main hydrates, whereas the grey scale lower than the biochar peak was the pores and higher than the peak of main hydration products should be the unreacted clinker. Therefore, the region (greyscale) near the boundary (~150–200) was assigned as the Ca-rich hydration products, which was similar to the observation in BSEM despite a lower resolution. After segmentation, the porous biochar particles (major one: 4.0 × 2.4 mm) could be observed (Fig. 9a) together with the wrapped hydration products (Fig. 9c). Although the resolution of the current X-CT did not allow a definitive differentiation of hydration products as done by the BSEM images, the as-segmented (Fig. S7c) Ca-rich layer can be isolated as shown in Fig. 9b. It is noticeable that this Ca-rich layer was not consecutive and uniform all over the biochar particle, which could probably depend on the local chemical environment (i.e., active functional groups) on its surface. When further evaluating the smaller biochar particles by noise-reducing algorithm, the pixelation of the 4 × 10 μm biochar (Fig. 10) was segmented. The micro-/meso-pores in the irregular biochar particles could be observed from the sides of the top (Fig. 10a) and the bottom (Fig. 10b). At the side-edge, the Ca-rich layer was closely attached to the biochar particle. In some regions, the Ca-layer was not directly connected to the biochar, which was consistent with the BSEM observation (Fig. 4).

4. Conclusions

An in-depth investigation of the ITZ between biochar and hardened Portland cement was carried out. The results showed that the significant ‘wall effect’ occurred at the side-edge of biochar connected via a layer of Ca-rich hydration products. The mineralogical composition of this Ca-rich layer mainly contained the C–S–H gel, CH, and S-AFm phases. In particular, the h-AFm (i.e., C_4AH_{19}) may form due to the comparatively high water-to-cement ratio in the ITZ and the concentrated C_3A-rich clinkers attracted by electrostatic interaction. This Ca-rich layer of hydration products can also be visualised by X-CT. Regarding the top-edge of biochar, other than the ‘dilution effect’, some air bubbles could be exchanged from the internal pores, which was detrimental to the mechanical strength. The deformation of biochar under load at the micro-scale was in the viscous-elastic mode, whereas the cement matrix exhibited the typical plastic-elastic mode. Owing to the good connection between biochar and hardened cement matrix, the ITZ possessed less plastic deformation during the nano-indentation. These deformations of unique regions could also be visually illustrated by the FEM simulation. The micro-mechanical behaviour could partially explain the higher compressive strength than previously expected in the literature.

Declaration of competing interest

The authors declare that they have no known competing financial interests or personal relationships that could have appeared to influence the work reported in this paper.

Data availability

Data will be made available on request.

Acknowledgement

The authors appreciate the financial support from the Hong Kong Green Tech Fund (GTF202020153).

Appendix A. Supplementary data

Supplementary data to this article can be found online at https://doi.org/10.1016/j.cemconcomp.2023.105004.

References

[1] N. Mac Dowell, et al., The role of CO_2 capture and utilization in mitigating climate change, Nat. Clim. Change 7 (4) (2017) 243–249.
[2] V. Masson-Delmotte, et al., Global warming of 1.5 C, IPCC Spl Rep. Impact. Global Warming. 1 (5) (2018).
[3] P.J.M. Monteiro, S.A. Miller, A. Horvath, Towards sustainable concrete, Nat. Mater. 16 (7) (2017) 698–699.
[4] S.A. Miller, F.C. Moore, Climate and health damages from global concrete production, Nat. Clim. Change 10 (5) (2020) 439–443.
[5] D.P. Van Vuuren, et al., Alternative pathways to the 1.5 C target reduce the need for negative emission technologies, Nat. Clim. Change 8 (5) (2018) 391–397.
[6] P. Fennell, et al., Cement and Steel—Nine Steps to Net Zero, Nature Publishing Group, 2022.
[7] L. Chen, et al., Biochar-augmented carbon-negative concrete, Chem. Eng. J. 431 (2022), 133946.
[8] A.D. Ellerman, F.J. Convery, Perthuis C. De, Pricing Carbon: the European Union Emissions Trading Scheme, Cambridge University Press, 2010.
[9] M. He, et al., Waste-derived biochar for water pollution control and sustainable development, Nat. Rev. Earth Environ. 3 (7) (2022) 444–460.
[10] R.D. Bergman, et al., Life cycle analysis of biochar [Chapter 3], in: Viktor Bruckman, Varol, Apaydin Esin, Basak Uzun, Jay Liu (Eds.), Biochar: A Regional Supply Chain Approach in View of Climate Change Mitigation, Cambridge University Press, Cambridge, UK, 2017, pp. 46–69.
[11] E.S. Azzi, E. Karltun, C. Sundberg, Prospective life cycle assessment of large-scale biochar production and use for negative emissions in Stockholm, Environ. Sci. Technol. 53 (14) (2019) 8466–8476.
[12] L. Mo, et al., Combined effects of biochar and MgO expansive additive on the autogenous shrinkage, internal relative humidity and compressive strength of cement pastes, Construct. Build. Mater. 229 (2019), 116877.
[13] D. Cuthbertson, et al., Biochar from residual biomass as a concrete filler for improved thermal and acoustic properties, Biomass Bioenergy 120 (2019) 77–83.
[14] Y.U. Kim, et al., Evaluation of thermal properties of phase change material-integrated artificial stone according to biochar loading content, Construct. Build. Mater. 305 (2021), 124682.
[15] F. Wu, Q. Yu, C. Liu, Durability of thermal insulating bio-based lightweight concrete: understanding of heat treatment on bio-aggregates, Construct. Build. Mater. 269 (2021), 121800.
[16] L. Wang, et al., The roles of biochar as green admixture for sediment-based construction products, Cement Concr. Compos. 104 (2019), 103348.
[17] L. Chen, et al., Roles of biochar in cement-based stabilization/solidification of municipal solid waste incineration fly ash, Chem. Eng. J. 430 (2022), 132972.
[18] Q. Wang, et al., Immobilization and recycling of contaminated marine sediments in cement-based materials incorporating iron-biochar composites, J. Hazard Mater. 435 (2022), 128971.
[19] Y.-X. Li, et al., A study on the relationship between porosity of the cement paste with mineral additives and compressive strength of mortar based on this paste, Cement Concr. Res. 36 (9) (2006) 1740–1743.
[20] K.L. Scrivener, Backscattered electron imaging of cementitious microstructures: understanding and quantification, Cement Concr. Compos. 26 (8) (2004) 935–945.
[21] K.L. Scrivener, A.K. Crumbie, P. Laugesen, The interfacial transition zone (ITZ) between cement paste and aggregate in concrete, Interface Sci. 12 (4) (2004) 411–421.
[22] W. Li, Z. Luo, Y. Gan, et al., Nanoscratch on mechanical properties of interfacial transition zones (ITZs) in fly ash-based geopolymer composites, Compos. Sci. Technol. 214 (2021), 109001.
[23] K. Wu, et al., Microstructural characterisation of ITZ in blended cement concretes and its relation to transport properties, Cement Concr. Res. 79 (2016) 243–256.
[24] K. Miyake, et al., The effect of pile-up and contact area on hardness test by nano-indentation, Jpn. J. Appl. Phys. 43 (7S) (2004) 4602.
[25] M.G. Maneiro, J. Rodríguez, Pile-up effect on nanoindentation tests with spherical–conical tips, Scripta Mater. 52 (7) (2005) 593–598.
[26] C. Shi, et al., Effects of indenter tilt on nanoindentation results of fused silica: an investigation by finite element analysis, Mater. Trans. 54 (6) (2013) 958–963.
[27] Z. Luo, W. Li, Y. Gan, et al., Nanoindentation on micromechanical properties and microstructure of geopolymer with nano-SiO2 and nano-TiO2, Cement Concr. Compos. 117 (2021), 103883.
[28] Z. Luo, W. Li, Y. Gan, et al., Maximum likelihood estimation for nanoindentation on sodium aluminosilicate hydrate gel of geopolymer under different silica modulus and curing conditions, Compos. B Eng. 198 (2020), 108185.
[29] J.J. Chen, et al., A Coupled nanoindentation/SEM-EDS study on low water/cement ratio Portland cement paste: evidence for C–S–H/$Ca(OH)_2$ nanocomposites, J. Am. Ceram. Soc. 93 (5) (2010) 1484–1493.
[30] X. Zhu, et al., Characterisation of pore structure development of alkali-activated slag cement during early hydration using electrical responses, Cement Concr. Compos. 89 (2018) 139–149.
[31] J. Maso, Interfacial Transition Zone in Concrete, CRC Press, 1996.
[32] P. Trtik, et al., 3D imaging of microstructure of spruce wood, J. Struct. Biol. 159 (1) (2007) 46–55.
[33] L. Wang, et al., Biochar aging: mechanisms, physicochemical changes, assessment, and implications for field applications, Environ. Sci. Technol. 54 (23) (2020) 14797–14814.
[34] G. Fang, M. Zhang, The evolution of interfacial transition zone in alkali-activated fly ash-slag concrete, Cement Concr. Res. 129 (2020), 105963.
[35] G. Fang, Q. Wang, M. Zhang, Micromechanical analysis of interfacial transition zone in alkali-activated fly ash-slag concrete, Cement Concr. Compos. 119 (2021), 103990.
[36] Y. Zhang, et al., Functional biochar synergistic solid/liquid-phase CO_2 capture: a review, Energy Fuel. 36 (6) (2022) 2945–2970.
[37] I.G. Richardson, S. Li, Composition and structure of an 18-year-old 5M KOH-activated ground granulated blast-furnace slag paste, Construct. Build. Mater. 168 (2018) 404–411.
[38] F. Yang, et al., Kaolinite enhances the stability of the dissolvable and undissolvable fractions of biochar via different mechanisms, Environ. Sci. Technol. 52 (15) (2018) 8321–8329.
[39] X. Kang, et al., Hydration of C3A/gypsum composites in the presence of graphene oxide, Mater. Today Commun. (2020) 23.
[40] N. Ukrainczyk, et al., Dehydration of a layered double hydroxide—C_2AH_8, Thermochim. Acta 464 (1–2) (2007) 7–15.
[41] I.G. Richardson, et al., Hydration of water- and alkali-activated white Portland cement pastes and blends with low-calcium pulverized fuel ash, Cement Concr. Res. 83 (2016) 1–18.
[42] I.G. Richardson, The nature of C-S-H in hardened cements, Cement Concr. Res. 29 (1999) 1131–1147.
[43] A.V. Girao, et al., Morphology and nanostructure C–S–H in white Portland cement–fly ash hydrated at 85°C, Adv. Appl. Ceram. 106 (6) (2007) 283–293.
[44] B.Z. Dilnesa, et al., Synthesis and characterization of hydrogarnet Ca3(AlxFe1−x)2(SiO4)y(OH)4(3−y), Cement Concr. Res. 59 (2014) 96–111.
[45] S. Joseph, J. Skibsted, Ö. Cizer, A quantitative study of the C3A hydration, Cement Concr. Res. 115 (2019) 145–159.
[46] Y. Sun, et al., Multifunctional iron-biochar composites for the removal of potentially toxic elements, inherent cations, and hetero-chloride from hydraulic fracturing wastewater, Environ. Int. 124 (2019) 521–532.
[47] Z. Lu, et al., Towards a further understanding of cement hydration in the presence of triethanolamine, Cement Concr. Res. 132 (2020), 106041.
[48] Z. Lu, et al., Effect of highly carboxylated colloidal polymers on cement hydration and interactions with calcium ions, Cement Concr. Res. 113 (2018) 140–153.
[49] K. Yoshioka, et al., Adsorption characteristics of superplasticizers on cement component minerals, Cement Concr. Res. 32 (10) (2002) 1507–1513.
[50] J. Plank, C. Hirsch, Impact of zeta potential of early cement hydration phases on superplasticizer adsorption, Cement Concr. Res. 37 (4) (2007) 537–542.
[51] W.C. Oliver, G.M. Pharr, An improved technique for determining hardness and elastic modulus using load and displacement sensing indentation experiments, J. Mater. Res. 7 (6) (1992) 1564–1583.
[52] G. Pharr, W.C. Oliver, F. Brotzen, On the generality of the relationship among contact stiffness, contact area, and elastic modulus during indentation, J. Mater. Res. 7 (3) (1992) 613–617.
[53] M.L. Oyen, R.F. Cook, A practical guide for analysis of nanoindentation data, J. Mech. Behav. Biomed. Mater. 2 (4) (2009) 396–407.
[54] G. Zickler, T. Schöberl, O. Paris, Mechanical properties of pyrolysed wood: a nanoindentation study, Phil. Mag. 86 (10) (2006) 1373–1386.
[55] O. Das, A.K. Sarmah, D. Bhattacharyya, Structure-mechanics property relationship of waste derived biochars, Sci. Total Environ. 538 (2015) 611–620.
[56] O. Das, A.K. Sarmah, D. Bhattacharyya, Nanoindentation assisted analysis of biochar added biocomposites, Compos. B Eng. 91 (2016) 219–227.
[57] C. Liang, et al., Ultra-light MXene aerogel/wood-derived porous carbon composites with wall-like "mortar/brick" structures for electromagnetic interference shielding, Sci. Bull. 65 (8) (2020) 616–622.
[58] M. Vandamme, F.J. Ulm, Nanoindentation investigation of creep properties of calcium silicate hydrates, Cement Concr. Res. 52 (2013) 38–52.
[59] J. Frech-Baronet, L. Sorelli, J.P. Charron, New evidences on the effect of the internal relative humidity on the creep and relaxation behaviour of a cement paste by micro-indentation techniques, Cement Concr. Res. 91 (2017) 39–51.

[60] Z. Luo, W. Li, P. Li, et al., Investigation on effect of nanosilica dispersion on the properties and microstructures of fly ash-based geopolymer composite, Construct. Build. Mater. 282 (2021), 122690.
[61] J. Li, W. Zhang, P.J.M. Monteiro, Preferred orientation of calcium aluminosilicate hydrate compacts: implications for creep and indentation, Cement Concr. Res. 143 (2021), 106371.
[62] K.L. Johnson, K.L. Johnson, Contact Mechanics, Cambridge university press, 1987.
[63] P. Lan, et al., A phenomenological elevated temperature friction model for viscoelastic polymer coatings based on nanoindentation, Tribol. Int. 119 (2018) 299–307.
[64] S. Liang, Y. Wei, Effects of water-to-cement ratio and curing age on microscopic creep and creep recovery of hardened cement pastes by microindentation, Cement Concr. Compos. 113 (2020), 103619.
[65] Y.-T. Cheng, C.-M. Cheng, Relationships between hardness, elastic modulus, and the work of indentation, Appl. Phys. Lett. 73 (5) (1998) 614–616.
[66] G. Fang, Q. Wang, M. Zhang, In-situ X-ray tomographic imaging of microstructure evolution of fly ash and slag particles in alkali-activated fly ash-slag paste, Compos. B Eng. 224 (2021), 109221.
[67] J.E. Vigor, et al., Automated correction for the movement of suspended particulate in microtomographic data, Chem. Eng. Sci. 223 (2020), 115736.